Mapping the subsurface structures and contacts using aeromagnetic data (case study: central and northern Egypt)

Ahmed Abdelwahed,[1*] Mohamed Gamal[2] and Ahmed Metwally[1]

[1]Lecturer, Geophysics Department, Faculty of Science, Cairo University, Giza, Egypt
[2]Assistant Professor, Geophysics Department, Faculty of Science, Cairo University, Giza, Egypt

Abstract

This paper represents the analysis and interpretation of the airborne magnetic data of central and northern Egypt to delineate the subsurface faults and other structures and also the tectonic framework of the area. First, the total observed magnetic field data was reduced to the north magnetic pole (RTP) and using the power spectrum, the regional and residual magnetic fields were separated using the Butterworth filter to isolate the anomalies caused by each of them. Then, the airborne magnetic data was subjected to several filters to enhance the signals from the different magnetic sources for better delineation and edge detection. Additionally, Euler deconvolution was applied to estimate the depth of the different magnetic sources.

The final outputs show a wide variety of magnetic anomalies reflecting different magnetic sources and subsurface features. The main subsurface structures are the linear NNW-SSE parallel to the Red Sea trend and the Gulf of Suez and the NE-SW faults and lineaments surrounding the basins in the northern and western area, the deeply rooted basic intrusions, and the depo-centers (basins) in the western and central parts of the area. Moreover, the area shows several basement uplifts and consequently faulted basins of different directions and displacements.

Corresponding author: wahmed@sci.cu.edu.eg

1   Introduction

The magnetic methods are widely used to detect and map the main geological features, structural trends and even the tectonic setting from the recorded magnetic anomalies (Dobrin and Savit, 1988; Nabighian et al., 2005; Nigm et al., 2015).

Aeromagnetic surveys are used to delineate the depth to the basement and the structures affecting them specially faults and other lineaments or contacts.

The subsurface of the northern and central parts of Egypt (Fig. 1) is characterized by a complicated system of Mesozoic rift basins (Hantar, 1990; Sehim, 1993; Bosworth et al., 2008; Dolson et al., 2014; Bosworth et al., 2015; Mostafa et al., 2018). They form a series of grabens trending E-W to ENE-WSW and NE-SW that originated in the Jurassic and continued subsidence through the Cretaceous, such as the Abu Gharadig, Alamein, Matruh, and Shoushan basins (Sultan and Halim, 1988; Emam et al., 1990; Taha, 1992; Moustafa, 2008; Bevan and Moustafa, 2012; Bosworth et al., 2015; Mostafa et al., 2018).
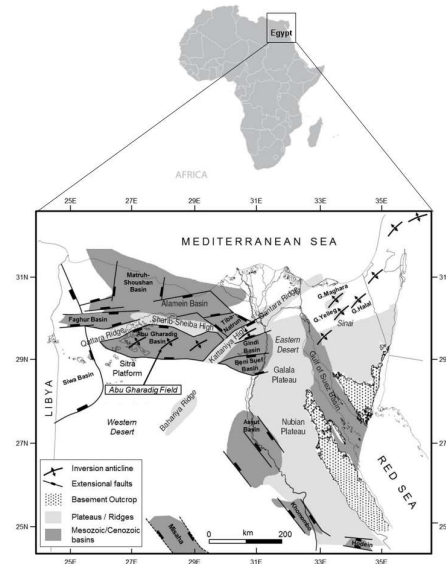
Figure 1. Complicated system of Mesozoic rift basins forming a series of grabens and half grabens (modified after Dolson et al., 2001; Bosworth et al., 2008; Moustafa, 2008; Bevan and Moustafa, 2012; Mostafa et al., 2018). The black rectangle represents the study area.
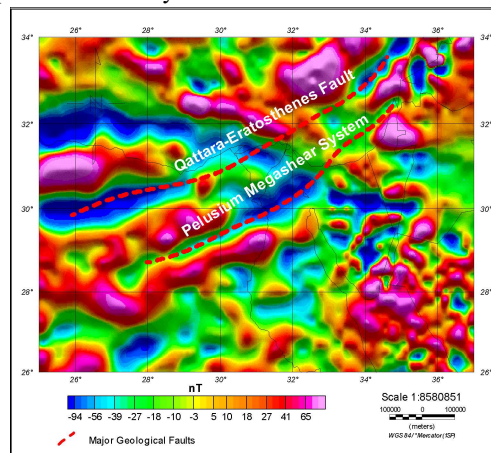
Figure 2. Total magnetic intensity (TMI) map of the northern and central parts of Egypt (EMAG2 project) (Maus et al., 2009).

The aim of this study is to map the subsurface structures in central and northern Egypt and define their main trends and directions via the analysis and interpretation of the acquired aeromagnetic data. The study area is located between latitudes 26°00'00" and 34°00'00" and longitudes 25°75'00" and 36°75'00". The Geomagnetic Reference Field was subtracted from the total magnetic intensity data, then it was transformed to the wave-number domain (Fig. 2).

The basement of northern and central Egypt consists mainly of granite, granodiorite and weakly deformed plutonic rocks. On the other hand, the southern basement is composed of mafic metavolcanics, gabbros, ultramafic rocks and associated meta sedimentary rocks, where the separating boundary between them is near Safaga (Stern et al., 1984; Cochran, 2005; Hamimi et al., 2020).

The basement rocks and basic intrusive geological bodies cause positive magnetic anomalies, while the sedimentary rocks and recent Quaternary acidic deposits cause relatively negative magnetic response or anomalies. The broad anomalies with gentle gradients indicate deeper magnetic sources, while sharp and narrow anomalies reflect shallower magnetic bodies.

2 Database specifications

The region of interest is covered by an area of about 1,056,000 km^2 using WGS-84 as a datum and Mercator (1SP) as a projection. The total intensity magnetic map is from the world wide project "Magnetic anomaly map of the world" (EMAG3) (Maus et al., 2009) with grid spacing of 3 km and scale of 1:8,580,851. EMAG3 is a first global magnetic anomaly grid which provides the base grid for the World Digital Magnetic Anomaly Map of the Commission of the World Geological Map. As reflected in the name, the resolution is 3 arc minute and the altitude is 5 km above geoid. It was compiled from satellite, marine, aeromagnetic and ground magnetic surveys.

3 Reduction to the north magnetic pole

The inclination effects in the observed total magnetic intensity map are removed by reducing the magnetic data to the north magnetic pole after applying Fourier transformation (Baranov, 1957; Baranov and Naudy, 1964).
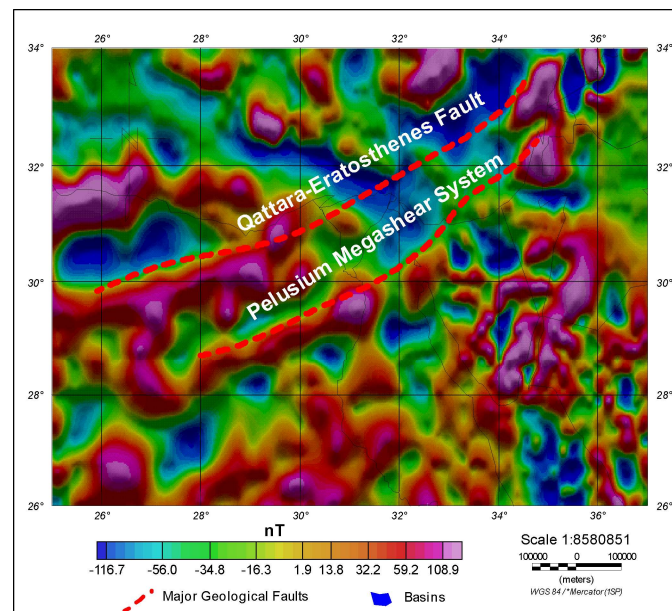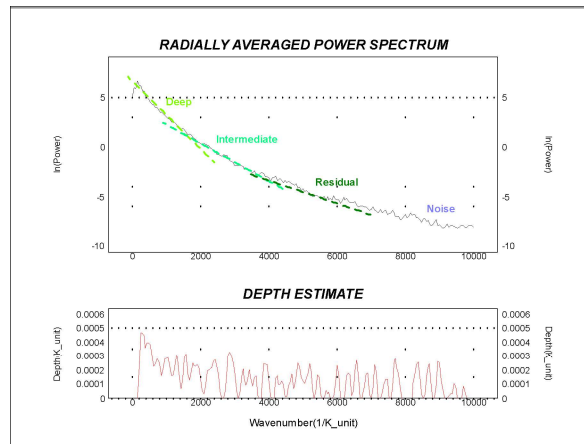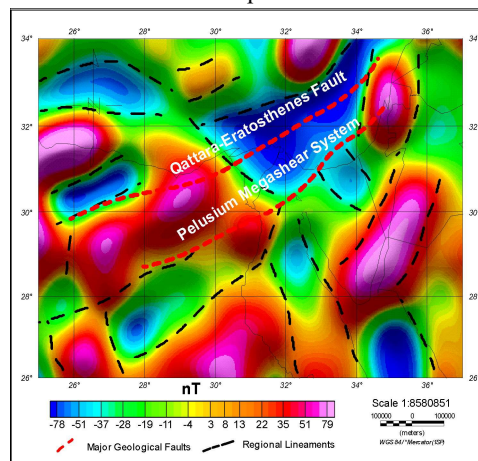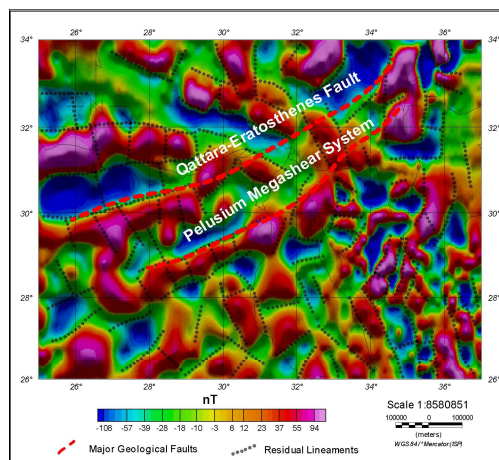

Figure 3. Reduced to the pole (RTP) aeromagnetic map.

Figure 4. Radial average power spectrum of the RTP magnetic intensity map showing the regional and residual components.

Figure 5. Regional magnetic component after separation from the RTP map with the expected interpreted

faults or contacts.

Figure 6. Residual magnetic component after separation from the RTP map with the expected interpreted

faults or contacts.
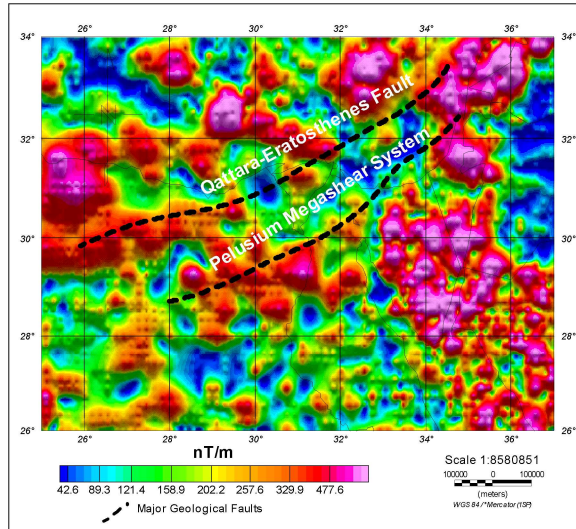
Figure 7. Analytic signal map. The peaks in the analytic signal amplitude show good match with two major faults**.**

This technique reduces the anomalies to as if they were observed or measured at the magnetic North Pole where the magnetic inclination is vertical (I=90°) as shown in Fig. 3.

4   Radially average power spectrum

The power spectrum of the data was calculated to examine the ranges of the frequencies revealed in the data so that we can separate the low frequencies regional anomalies from the high frequency residual anomalies. The power spectrum is often observed to be broken up into a series of straight line segments. A typical energy spectrum for magnetic data may exhibit three parts to the spectrum: a deep source component (regional), intermediate and shallow source components (residual), and a noise component (Nettleton, 1976; Al-Badani, 2018). Fig. 4 shows the calculated power spectrum with regional and residual components.

The regional map (Fig. 5) exhibits the broad anomalies which reflect the deep seated magnetic sources of the basement, while the residual map (Fig. 6) demonstrates the local anomalies related to the shallow structural features.

5   Analytic signal

The analytic signal is a very useful technique as it outlines the magnetic sources. It is not affected by the magnetic inclination and equalizes the signal amplitudes, but the peaks of the transformed data are positioned directly over body's center. This method is not an edge detector method (Cooper and Cowan, 2008). It is represented as follows:

$$A(x, y) = \frac{\partial \Delta T}{\partial x} i + \frac{\partial \Delta T}{\partial y} j + \frac{\partial \Delta T}{\partial z} k \qquad (1)$$

where i, j, and k are unit vectors in the x, y, and z directions, respectively.

The amplitude of the analytic signal represents the square root of the squared sum of the two horizontal derivatives and the vertical derivative of the magnetic field (Macleod et al., 2000; Al-Badani, 2018). It is defined as follows:

$$|A(x, y)|^2 = \sqrt{(\frac{\partial \Delta T}{\partial x})^2 + (\frac{\partial \Delta T}{\partial y})^2 + (\frac{\partial \Delta T}{\partial z})^2} \qquad (2)$$

This signal shows maximum over magnetization contrasts which represents the outlines of magnetic sources and marks the edges of the magnetized sources. Fig. 7 shows the constructed map after calculating the analytic signal.

The analytic signal technique (Nabighian, 1972; Roest et al., 1992) suggests that the
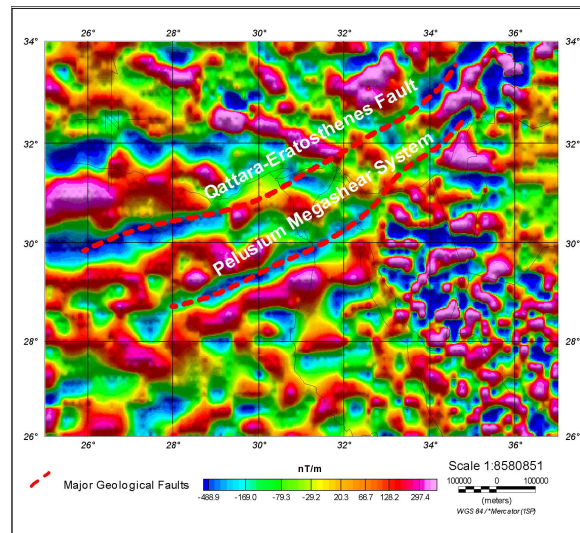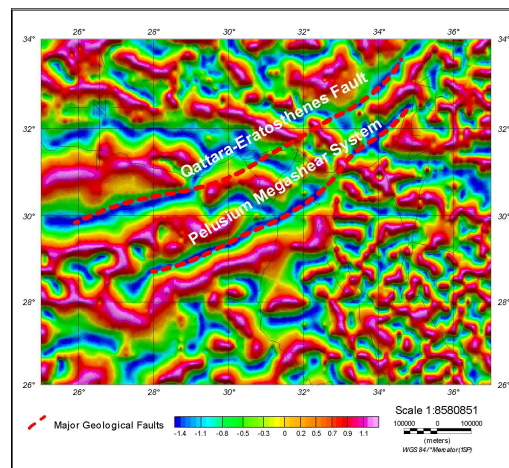
Figure 8. First vertical derivative (FVD) map**.**

Figure 9. Tilt derivative (TDR) map (Gamal, 2013)**.**

sources are separate dipping contacts between bulk geological bodies. Peaks in the analytic signal amplitude are used to delineate the contacts and provide their strike directions.

6   First vertical derivative

The first vertical derivative (Fig. 8) emphasizes the shallow component of the source geology while still leaving some middle wavelengths and eliminating very long wavelengths (Blakely, 1995). The edges of anomalies will become sharper or clearer if derivative operators applied to the data can be derived mathematically by:

$$VDR = -\frac{\partial \text{T}}{\partial \text{Z}} \tag{3}$$

where (∂ T/ ∂ Z) is the vertical derivative of gravity or RTP anomalies in Z direction.

7   Tilt derivative (TDR)

The tilt derivative technique is very useful in detecting and enhancing the edges of the magnetized subsurface features or bodies (Miller and Singh, 1994; Salem et al., 2007; Salem et al., 2008; Hinze et al., 2013; Al-Badani and Al-Wathaf, 2018). Fig. 9 shows the tilt derivative (TDR) map for this case study. It is defined as:

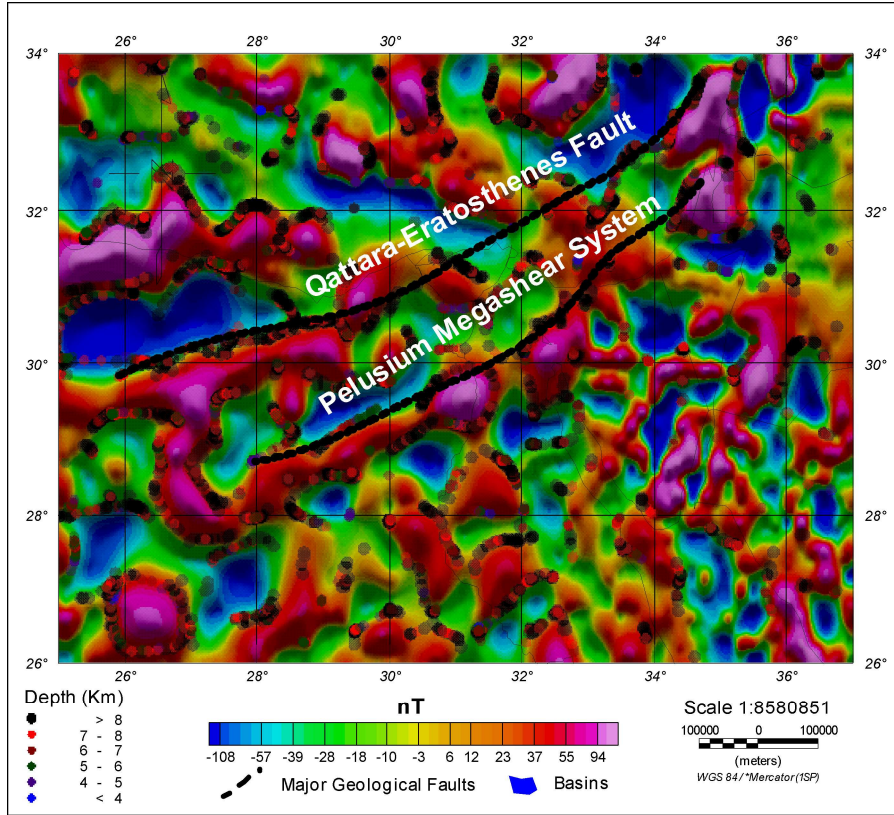$$TDR = tan^{-1}\frac{VDR}{THDR} \tag{4}$$

Figure 11. Euler solutions (SI=0) superimposed on the residual magnetic map.

8   Horizontal gradient

The horizontal gradient (HG) which represents a simple approach to locate linear features such as faults or even contacts from magnetic field data (Cordell and Grauch, 1982, 1985), peaks over the edges and is zero over the body. It is defined as follows:

$$HG(x,y) = \sqrt{(\frac{\partial M}{\partial x})^2 + (\frac{\partial M}{\partial y})^2} \qquad (5)$$

where M(x,y) is the magnetic field. The horizontal gradient (Fig. 10) is used to define the spatial location of the magnetic discontinuities on the residual RTP map. The main advantage of this technique is its ability to locate edges of different magnetic sources, faults, contacts and other high frequency features in the magnetic data (Nigm et al., 2015; Al-Badani and Al-Wathaf, 2018).

The horizontal gradient (HG) map (Fig. 10) is used to precisely detect the edges of the subsurface magnetic bodies, where the horizontal gradient peaks are interpreted as the boundaries of the causative magnetic structures.

9   Euler deconvolution

This technique is used for depth estimation (Thompson, 1982) based on the assumption that the magnetic fields of the localized features or bodies are homogeneous functions (Reid et al., 1990) of the magnetized source subsurface coordinates and follows Euler's equation:

$$(x - x_o)\frac{\partial \Delta T}{\partial x} + (y - y_o)\frac{\partial \Delta T}{\partial y} +$$

$$(z - z_o)\frac{\partial \Delta T}{\partial z} = -SI\Delta T \qquad (6)$$

where (x, y, z) is the position at which the total field anomaly is ΔT, arising from a

source at position (x_0, y_0, z_0). SI is the structure index based on the geometry of the source body (Thompson, 1982) and equals to 0 or 0.5 for faults and geological contacts (Reid et al., 1990). The calculated depths to the subsurface structural features are shown in Fig. 11. Euler deconvolution

is used to determine the depth of the determined geological contacts at their positions where the selected structural index (SI) equals to zero which is commonly used for the contacts. The results are superimposed on the residual
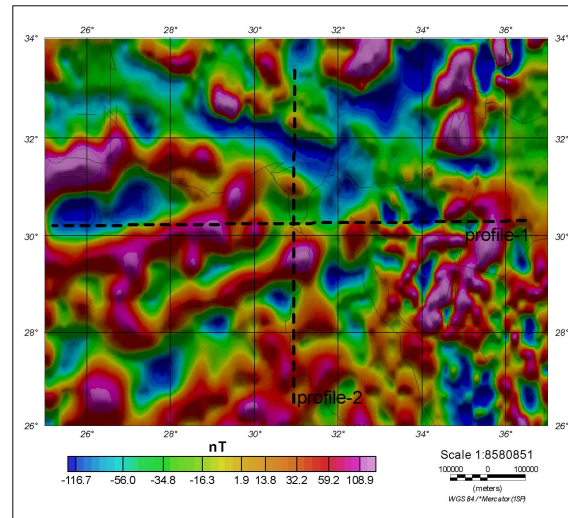
Figure 12. Reduced to the pole (RTP) aeromagnetic map with the two perpendicular profiles used for the magnetic modeling.
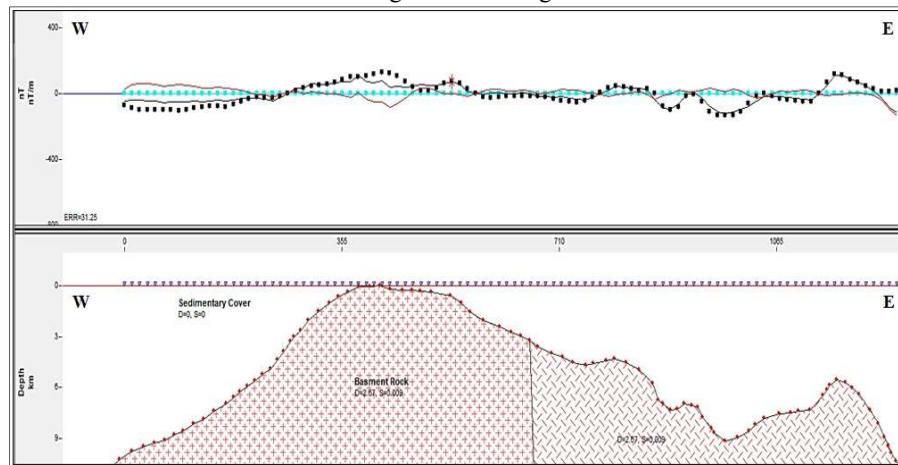
Figure 13. Magnetic modeling along profile-1. The solid black curve and the dotted black curve represent the calculated and observed data, respectively. The solid red curve represents the error.

magnetic map (Fig. 11) showing good match and consistency between them.

10 Magnetic modeling

Abrupt changes in the magnetic intensity indicate the presence of several subsurface structures and contacts across the study

area. Two perpendicular magnetic models were constructed using the digitized RTP magnetic data (Figure. 12).

Profile-1 extends horizontally from west to east while profile-2 extends vertically from north to south. The magnetic field is constructed through iterative calculation

for the estimated geological model until a good fit between the observed and calculated data is acquired (El Sirafe, 1986; Nigm et al., 2015).

The 2D forward modeling was constructed using the Geosoft GM-SYS program (Gemperle et al., 1991; Wen and Bevis, 1987; Mukhopadhyay et al., 2021).

Both models (Figs. 13 and 14) show good fit between the observed and calculated anomalies with low RMS error.

11 Interpretation and discussion

The aim of this study is to delineate the subsurface faults and other structures and
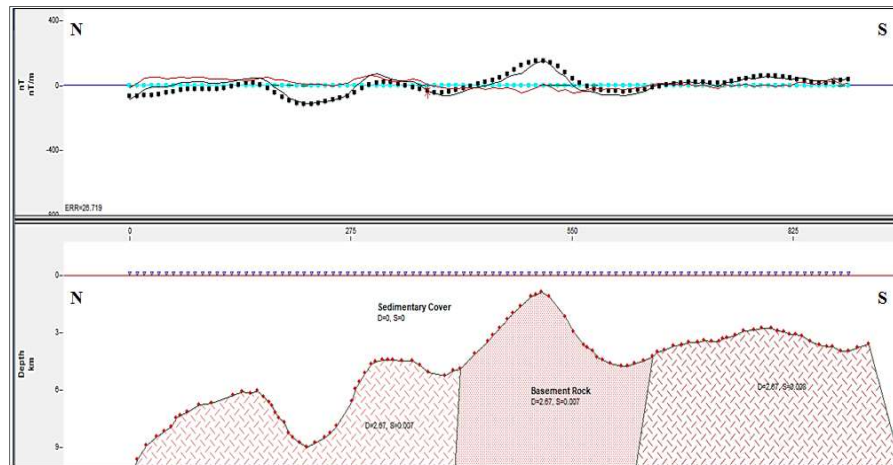
Figure 14. Magnetic modeling along profile-2. The solid black curve and the dotted black curve represent the calculated and observed data, respectively. The solid red curve represents the error.

also the tectonic framework of central and northern Egypt using the airborne magnetic data. Furthermore, using Euler deconvolution, the depth of the edges of the causative magnetic sources was estimated. The interpreted magnetic anomalies are due to the depth, shape and thickness of the subsurface magnetic sources in the study area.

The regional magnetic map shows the main platform area and the uplifts at the high magnetic reliefs with the associated main basins at the low magnetic relief. The contacts between the high and low magnetic responses are interpreted as the estimated faults between them. From the residual map, more detailed magnetic anomalies were observed with different magnitudes and sizes. This reflects the basins in the area due to the subsurface structures and faults, so the main basins detected on the regional map are dissected by faults into local basins which could be

obviously detected on the residual map. According to Dobrin and Savit (1988), the detected basin is characterized by gentle and smooth contours and relatively low magnetic response, while the surrounding area and other geological uplifts show steep slopes and high magnetic anomalies.

The analytic signal map (Fig. 7) shows maximum response over the magnetic contacts, independent of the ambient magnetic field and source of magnetization directions. Peaks in the analytic signal amplitude are used to delineate the contacts and provide their strike directions. The calculated map shows good matching and coherency with the major geological faults.

The local magnetic sources detected are clearly enhanced in the FVD map (Fig. 8). The TDR map (Fig. 9) confirms the same features and provides more evidence on the proposed interpretation. The horizontal gradient (HG) map (Fig. 10) is used to

precisely detect the edges of the subsurface magnetic bodies where the horizontal gradient peaks are interpreted as the boundaries of the causative magnetic structures.

Euler deconvolution is used to determine the depth of the determined geological contacts at their positions where the selected structural index (SI) equals to zero which is commonly used for the contacts. The results superimposed on the residual magnetic map (Fig. 11) show good match and consistency between them.

The two perpendicular models (Figs. 13 and 14) show that the basement relief differs in depth and susceptibility from
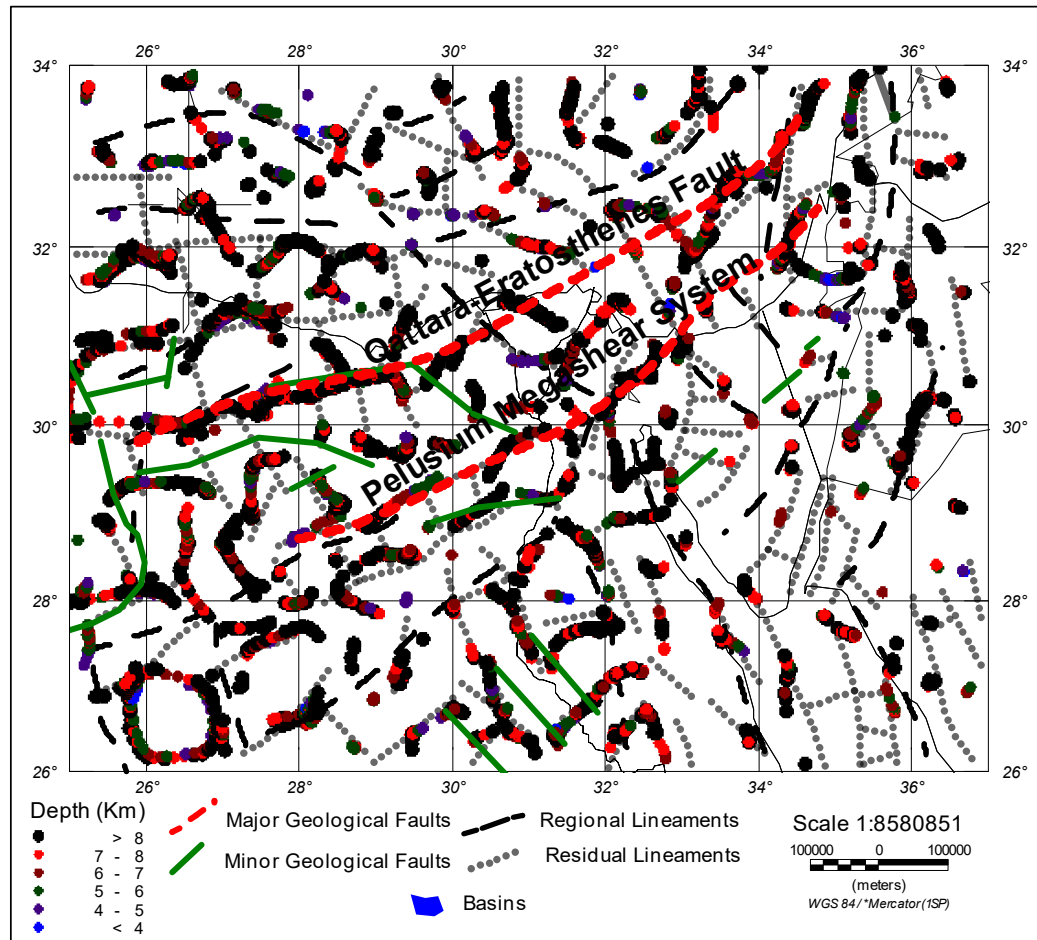
Figure 15. The estimated subsurface structures (regional and residual faults or lineaments) from this case study with the major and minor faults superimposed from the previous geological studies and maps (modified after Dolson et al., 2001; Bosworth et al., 2008; Moustafa, 2008; Bevan and Moustafa, 2012; Mostafa et al., 2018).

subsurface block to another with the estimated thickness of the associated sedimentary basin.

Fig. 15 represents a summary for the outputs and the estimated subsurface structures and contacts from this case study compared with the major and minor faults superimposed from the previous geological studies or maps. Both of them show consistency.

In this study, several methods were used for detection of the expected faults and lineaments. Figs. 7, 8, 9 and 10 show high degree of consistency with very little differences which might be due to the

depths, locations and sizes of the magnetized sources and the contacts between them. Fig. 15 displays all the interpreted (regional, major and minor) faults and lineaments.

12   Conclusion

In this case study aeromagnetic data were used to delineate and map the subsurface features in central and northern Egypt. Reduction to the pole (RTP) was applied on the observed total magnetic intensity map as the first step of the analysis and processing. The next step was separation of the regional and residual magnetic fields based on the radially averaged power spectrum which consists of three main segments (trends): regional segment, residual segment and noise.

The final outputs show a wide variety of magnetic anomalies reflecting different magnetic sources and subsurface features. The main subsurface structures are the linear NNW-SSE parallel to the Red Sea trend and the Gulf of Suez and the NE-SW faults and lineaments surrounding the basins in the northern and western area, the deeply rooted basic intrusions, and the depo-centers (basins) in the western and central parts of the area. Moreover, the area shows several basement uplifts and consequently faulted basins of different directions and displacements.

The analytic signal and the tilt derivative techniques TDR were used as edge detection methods. Both techniques agreed with each other. The local magnetic sources detected are clearly resolved by the FVD filter. The horizontal gradient (HG) map was used to detect the edges of the boundaries of the causative magnetic structures.
Euler deconvolution was used for depth determination of the interpreted geological contacts or features. The results superimposed on the residual magnetic map show a good agreement between both of them.
The variation in depth may be related to

many different structural elements in several directions causing some blocks to be deeper than the surrounding in a system splitting the regional main basins into local smaller sub-basins.

The constructed models illustrate that the basement relief differs in depth and also susceptibility from subsurface block to another with the estimated thickness of the sedimentary cover above each of them.

References

Al-Badani, M. A., and Al-Wathaf, Y. M., 2018, Using the aeromagnetic data for mapping the basement depth and contact locations, at southern part of Tihamah region, western Yemen: Egyptian Journal of Petroleum, **27**, 485–495.

Baranov, V., 1957, A new method for interpretation of aeromagnetic maps; pseudo-gravimetric anomalies: Geophysics, **22**, 359–383.

Baranov, V., and Naudy, H., 1964, Numerical calculation of the formula of reduction to the magnetic pole: Geophysics, **29**, 67–79.

Bevan, T. G., and Moustafa, A. R., 2012, Inverted rift-basins of northern Egypt, in Roberts, D., and Bally, A., eds., Regional Geology and Tectonics: Phanerozoic Rift Systems and Sedimentary Basins: Elsevier, 482–507, https://doi.org/10.1016/B978-0-444-56356-9.00018-3.

Blakely, R. J., 1995, Potential Theory in Gravity and Magnetic Applications: Cambridge University Press, Cambridge.

Bosworth, W., Abrams, M. A., Drummond, M., and Thompson, M., 2015, Jurassic rift initiation source rock in the Western Desert, Egypt—relevance to exploration in other continental rift systems: Proceeding of 34th Annual GCS-SEPM Foundation Bob F. Perkins Research Conference, Petroleum Systems in "rift" basins, 615–650.

Bosworth, W., El-Hawat, A. S., Helgeson, D. E., and Burke, K., 2008, Cyrenaican

"shock absorber" and associated inversion strain shadow in the collision zone of northeast Africa: Geology, **36**, 695–698,
https://doi.org/10.1130/G24909A.1.

Cochran, J. R., 2005, Northern Red Sea: Nucleation of an oceanic spreading center within a continental rift: Geochemistry, Geophysics, Geosystems, **6**, Q03006,
doi.org/10.1029/2004gc000826.

Cordell, L., and Grauch, V. J. S., 1982, Mapping basement magnetization zones from aeromagnetic data in the San Juan Basin, New Mexico: Society of Exploration Geophysicists, 52nd Annual Meeting, Abstracts and Bibliographies, 246–247.

Cordell, L., and Grauch, V. J. S., 1985, Mapping basement magnetization zones from aeromagnetic data in the San Juan basin, New Mexico, in Hinze, W. J., ed., The utility of regional gravity and magnetic anomaly maps: Society of Exploration Geophysicists, 181–197.

Dobrin, M. B., and Savit, C. H., 1988, Introduction to geophysical prospecting, 4th edition: McGraw-Hill Book Company, New York.

Dolson, J. C., Atta, M., Blanchard, D. C., Sehim, A., and Villinski, J., 2014, Egypt's future petroleum resources: a revised look into the 21st century: American Association of Petroleum Geologists Memoir, **106**, 143-178, doi.org/10.1036/13431856M106713.

Dolson, J. C., Shann, M. V., Matbouly, S. I., Hammouda, H., and Rashed, R. M., 2001, Egypt in the twenty first century: Petroleum potential in offshore trends: GeoArabia, **6**, 211–230.

El Sirafe, A. M., 1986, Application of aeromagnetic, aeroradiometric and gravimetric survey data in the interpretation of the geology of Cairo-Bahariya area, Northwestern Desert, Egypt: PhD. Thesis, AinShams University.

Emam, A., Dishopp, D., and Dunderdale,

I., 1990, The structural setting of the central Western Desert, Egypt: Proceedings of the 10th EGPC Petroleum Exploration and Production Conference, Cairo, Egypt, 30–70.

Gamal, M. A., 2013 Trusthfulness of the existence of the pelusium megashear fault system, east of Cairo, Egypt: Int. J. Geosci., **4**, 212-227.

Hamimi, Z., El-Barkooky, A., Frías, J. M., Fritz, H., and Abd El-Rahman, Y., 2020, Geology of Egypt: Springer Nature Switzerland AG.

Hantar, G., 1990, North western desert, in Said, R., ed., Geology of Egypt: August Aime Balkema Publishers, Rotterdam, Netherlands, 293–327.

Hinze, W. J., Von Frese, R. R. B., and Saad, A. H., 2013, Gravity and Magnetic Exploration Principles, Practices, and Applications: Cambridge University Press, New York.

MacLeod, I. N., Jones, K., and Dai, T. F., 2000, 3-D analytic signal in the interpretation of total magnetic field data at low magnetic latitudes: Research papers Geosoft Inc.

Maus, S., Barckhausen, U., Berkenbosch, H. et al., 2009, EMAG2: A 2-arc min resolution Earth Magnetic Anomaly Grid compiled from satellite, airborne, and marine magnetic measurements: Geochemistry, Geophysics, Geosystems, **10**(8), Q08005, doi: 10.1029/2009GC002471.

Miller, H. G., and Singh, V., 1994, Potential field tilt—a new concept for location of potential field sources: Journal of Applied Geophysics, **32**, 213–217.

Mostafa, A. A., Khadrah, A. M. A., and Refaat, A. A., 2018, Impact of diagenesis on reservoir quality evolution of the late Cenomanian Abu Roash "G" Member in the Sitra field, North Western Desert, Egypt: Marine and Petroleum Geology, doi:10.1016/j.marpetgeo.2018.05.003.

Moustafa, A. R., 2008, Mesozoic-Cenozoic basin evolution in the northern

Western Desert of Egypt, in Salem, M., El-Arnauti, A., Saleh, A., eds.: 3rd Symposium on the Sedimentary Basins of Libya, The Geology of East Libya, 29–46.

Mukhopadhyay, M., Saibi, H., Elawadi, E., and Al-Arifi, N., 2021, Pulsed emplacement under the Uyaijah granite ring structure, eastern Saudi Arabia – results from 3D gravity-magnetic inversion: Arabian Journal of Geosciences, **14**, 2199.

Nabighian, M. N., 1972, The analytic signal of two-dimensional magnetic bodies with the polygonal cross-section: its properties and use for automated anomaly interpretation: Geophysics, **37**(3), 507–517.

Nettleton, L. L., 1976, Gravity and Magnetics in Oil Prospecting: McGraw-Hill Book Co.

Nigm, A. A., ElKhodary, S. T., Elgendi, N. H., and Abdelwahab, F. M., 2015, Mapping the subsurface structural features of Al-Laqitah area, Central Eastern Desert of Egypt using aeromagnetic data: Arabian Journal of Geosciences, **8**, 3537–3549, doi: 10.1007/s12517-014-1444-5.

Reid, A. B., Allsop, J. M., Granser, H., Millett, A. J., and Somerton, I. W., 1990, Magnetic interpretation in three dimensions using Euler deconvolution: Geophysics, **55**, 80–91.

Roest, W. R., Verhoef, J., and Pilkington, M., 1992, Magnetic interpretation using the 3-D analytic signal: Geophysics, **57**(1), 116–125.

Salem, A., Williams, S., Fairhead, J., Ravat, D., and Smith, R., 2007, Tilt-depth method: a simple depth estimation method using first-order magnetic derivatives: The Leading Edge, **26**, 1502–1505.

Salem, A., Williams, S., Fairhead, D., Smith, R., and Ravat, D., 2008, Interpretation of magnetic data using tilt-angle derivatives: Geophysics, **73**, L1–L10.

Sehim, A., 1993, Cretaceous tectonics in Egypt: Egyptian Journal of Geology, **37**, 335–372.

Stern, R. J., Gottfried, D., and Hedge, C. E., 1984, Late Precambrian rifting and crustal evolution in the Northeastern Desert of Egypt: Geology, **12**, 168–172.

Sultan, N., and Halim, M. A., 1988, Tectonic framework of Northern Western Desert, Egypt and its effect on hydrocarbon accumulations: Proceedings of the 9th EGPC Petroleum Exploration and Production Conference, Cairo, Egypt, 1–19.

Taha, M. A., 1992, Mesozoic rift basins in Egypt: their southern extension and impact on future exploration: Proceedings of the 11th EGPC Petroleum Exploration and Production Conference, Cairo, Egypt, 1–19.

Thompson, D. T., 1982, EULDPH-A technique for making computer assisted depth estimates for magnetic data: Geophysics, **47**, 31–37.

Wen, I. J., and Bevis, M., 1987, Computing the gravitational and magnetic anomalies due to a polygon: Algorithms and Fortran subroutines: Geophysics, **52**, 232–238.